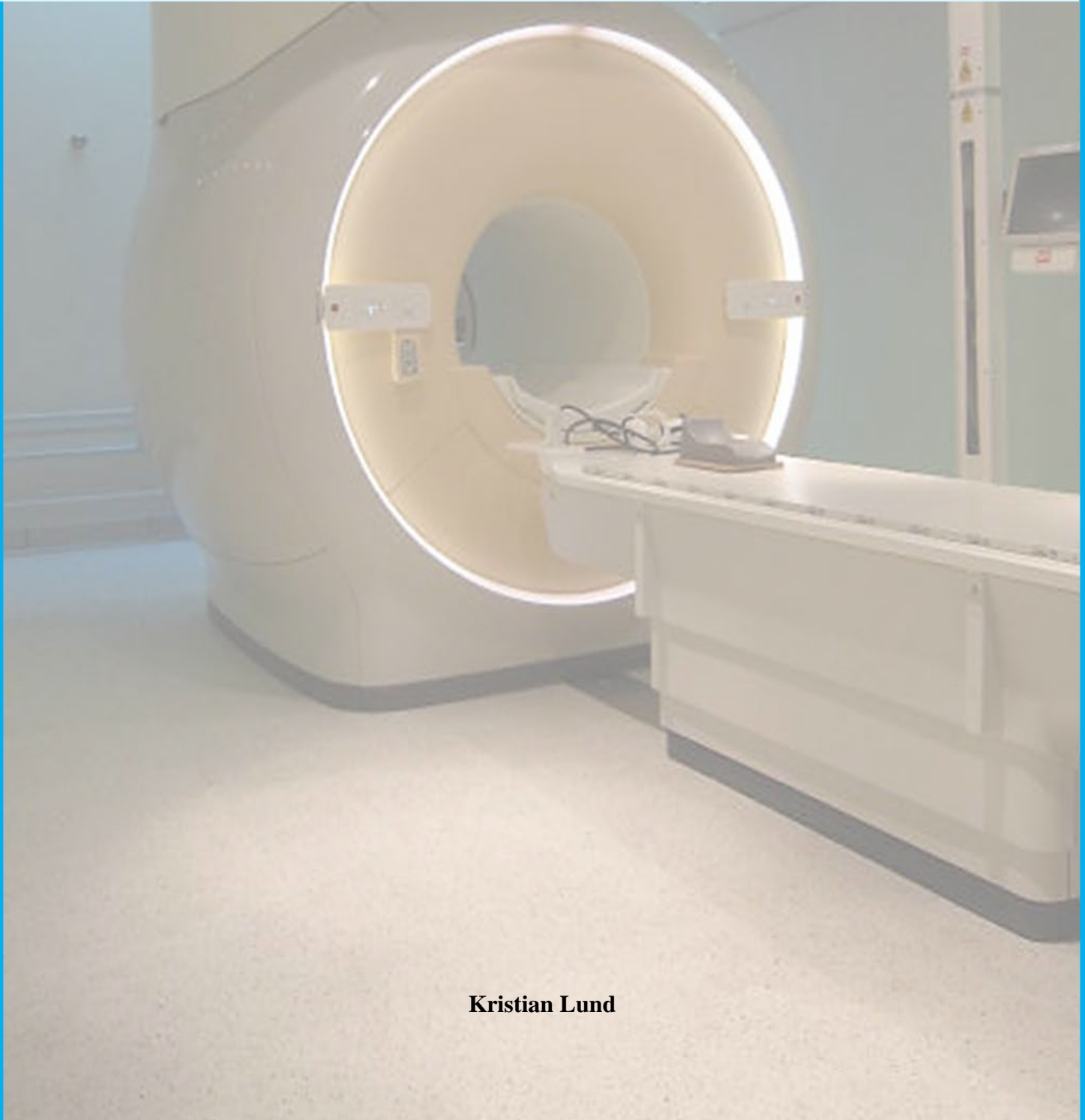


Aalborg University 03.06.2014

**CLINICAL
SCIENCE AND
TECHNOLOGY
4. SEMESTER**

Evaluating the Reliability and Precision of 6° and 16° Flip Angles Compared to Inversion Recovery When Generating T1 Relaxation Maps in MRI on a 3.0T Scanner in Relation to Cerebral Cancer.

Kristian Lund



Title: Evaluating the Reliability and Precision of 6° and 16° Flip Angles Compared to Inversion Recovery When Generating T1 Relaxation Maps in MRI on a 3.0T Scanner in Relation to Cerebral Cancer.

Theme: Clinical Science and Technology

Project period: 3/2 – 2014 to 3/6 - 2014

Project group: 14gr1096

Summary:

Participants:

Kristian Lund

Supervisors:

Carsten Dahl Mørch

Issue number printed: 2

Pages: 53

Appendix number: 8

Finished: 3/6 - 2014

Glioblastoma multiforme is a highly lethal subtype of cerebral cancers, and surgery, chemotherapy and radiation therapy is used as treatment. Functional Magnetic Resonance Imaging (MRI) scans such as Dynamic Contrast-Enhanced (DCE) MRI can be used to assess the effects of the treatments, but quantification of DCE-MRI images is problematic. To address this issue, MRI relaxation maps can be constructed, using methods like Variable Flip Angle (VFA) and Inversion Recovery (IR). A predetermined VFA method was tested and compared to the IR golden standard on six phantoms containing distilled water and different concentrations of the contrast agent Dotarem. All phantoms were scanned with both the VFA and IR technique three times and relaxation maps were created and compared in MatLab and the image software solution Imalytics. Coefficient of Variance (CV) and Intraclass Correlation Coefficient (ICC) were used, and visualized with a graph/Bland-Altman plots. SPSS was used for ICC calculations. For IR, a CV=0,82% was calculated, and for VFA, a CV=12,15% was calculated. For IR, an ICC=1 (CI: 1/1) for single measures was found, and for VFA, an ICC=0,723 (CI: 0,266/0,950) for single measures was found, using a Two-Way Mixed ICC method with absolute agreement analysis setting. A possible outlier likely contaminated the sample, though it was not excluded since it could not be ascertained with certainty that it was a true outlier.

Dansk Resume

Glioblastoma multiforme (GBM) er en ekstrem dødelig cerebral cancer, og forbindes med vanskeligheder i forhold til effektiv vurdering af effekten fra kemoterapeutiske stoffer. Et kemopræparat der bruges imod GBM er Bevacizumab, som virker ved at hæmme dannelsen af nye blodkar, samt nedbryde nydannede blodkar omkring tumoren. GBM tumoren er i stand til at stimulere kroppen til at danne nye blodkar som fører ind til tumoren og derved øge tumorens optag af energi fra blodbanen, samt giver tumoren mulighed for at sprede sig til andre steder i kroppen. Ved at benytte sig af en skanningsteknik kaldet T1 Dynamic Contrast-Enhanced Magnetic Resonance Imaging (DCE-MRI), kan man, via indsprøjtning af intravenøs kontrast, visualisere de hæmodynamiske forhold, såsom blodgennemstrømning og permeabilitet, for disse blodkar samt det omkringliggende væv. De signalintensiteter som kan ses på disse billeder er dog ikke i overensstemmelse med den faktiske koncentration af kontraststoffet i vævet, hvilket vanskeliggør kvantificering af billederne. For at kompensere for dette, kan der skabes T1 relaxationsmaps. Disse maps består af en række billeder som viser den sande signalintensitet i det skannede objekt. Disse T1 maps kan derefter bruges til at korrigere de oprindelige DCE-MRI billeder, således at der opnås sande signalintensiteter på disse billeder. På Afdelingen for Medicinsk Fysik på Aalborg Universitetshospital kører der flere projekter omhandlende DCE-MRI skanninger af cerebral cancer, og en metode til at skabe fungerende T1 maps ville være af værdi for disse projekter. Skabelsen af T1 maps er udfordrende, da forskellige studier rapporterer om forskellige resultater selvom de samme metoder og den samme skannertype benyttes.

I dette projekt vil en 3.0T skanner blive brugt til at skabe T1 maps, baseret på en prædefineret skanningsprotokol. Denne skanningsprotokol er baseret på flip angle princippet, og resultaterne fra den vil blive sammenlignet med inversion recovery skanninger. Inversion recovery skanninger betragtes som den gyldne standard indenfor T1 map generering. Resultaterne vil blive sammenlignet via varians koefficienter og intraclass correlation målinger, samt visualiseret v.h.a. en graf og to Bland-Altman plots. For varians koefficienten blev resultaterne: flip angle: $CV = 12.15$; inversion recovery: $CV = 0,82$. For intraclass correlation blev resultaterne: flip angle: $ICC = 0,723$; inversion recovery: $ICC = 1$. Resultaterne bærer dog præg af tilstedeværelsen af en mulig outlier, hvilket kan have kontamineret datasættet. En ekstra analyse blev udført, hvor denne mulige outlier var ekskluderet.

Table of Contents

1.0 Preface.....	1
2.0 Reading guide	2
3.0 Introduction.....	3
4.0 Background	4
4.1 Magnetic Resonance Imaging and Cerebral Cancer.....	4
4.2 Dynamic Contrast-Enhanced Magnetic Resonance Imaging.....	5
4.3 Magnetic Resonance Imaging mapping.....	6
4.4 Relevance	6
5.0 Study Aim	7
6.0 Theory	7
6.1 Basic Principles of Magnetic Resonance Imaging.....	7
6.2 T1 and T2 Relaxation.....	9
6.3 Contrast Agents.....	10
6.4 T1 Maps	11
6.4.1 Inversion Recovery Technique	11
6.4.2 Variable Flip Angle Technique.....	12
6.5 Dynamic Contrast-Enhanced Magnetic Resonance Imaging.....	13
6.6 The K^{trans} Parameter	13
7.0 Method	14
7.1 Study Design.....	14
7.2 Magnetic Resonance Imaging Contrast Agent.....	15
7.3 MatLab Processes	15
7.4 Imalytics.....	17
7.5 Statistical Analysis.....	18

7.5.1 Intraclass Correlation Coefficient	18
7.5.2 Coefficient of Variation	19
7.5.3 Bland-Altman Plots.....	20
7.5.4 Relaxation Time Graph.....	20
8.0 Results.....	21
8.1 Intraclass Correlation Coefficient and Coefficient of Variation.....	21
8.2 Additional Analyses	21
8.2 Bland-Altman Plots.....	23
8.3 Relaxation Time Graph.....	25
9.0 Discussion	26
9.1 Possible Outlier Evaluation.....	26
9.2 Coefficient of Variation	26
9.3 Intraclass Correlation Coefficient	27
9.3 Results Comparison	28
9.4 Radio Frequency Field Inhomogeneity.....	29
9.5 Choice of Flip Angles	29
9.6 Alternative Scanning Methods.....	30
9.7 Imalytics.....	31
10.0 Conclusion	31
11.0 Future Prospects	32
12.0 References.....	34

1.0 Preface

This master thesis was written by Kristian Lund, master student in Clinical Science and Technology at the School of Medicine and Health, Aalborg University. The project was created from February 3rd to June 3rd 2014, and was conducted in collaboration with The Department of Medical Physics at Aalborg University Hospital. The author of this report did not personally receive any form of funds or any other type of compensation.

I would like to thank my internal and external supervisors, Carsten Dahl Mørch and Jesper Carl, for their excellent guidance and feedback, and for giving me the opportunity to work on this exciting project. I would also like to extend my gratitude to Søren Ravn and Dennis Tideman Arp for all their assistance throughout the project period.

Kristian Lund

2.0 Reading guide

This report is primarily intended for my supervisors and The Department of Medical Physics at Aalborg University Hospital. Secondly it is intended for other interested parties.

The report utilizes the Vancouver reference system, and references to pictures, tables, graphs, figures and the appendix will appear throughout the report. References placed before a period indicate that the reference only applies to the sentence within which it is placed, whereas references placed after a period refer to the entire section of text preceding it, or up to the previous reference. References to websites will contain information about the date the site was visited as well as the last time the site was revised if the information is available.

3.0 Introduction

Glioblastoma multiforme (GBM) is a highly lethal brain cancer type, and is associated with difficulties regarding effect assessment of chemotherapeutic drugs. One such drug which is used to treat GBM is Bevacizumab, which works by reducing the creation of blood vessels leading to the tumor and causing regression of newly formed blood vessels near the tumor. (1) The GBM tumor is able to stimulate the body to create new blood vessels leading into the tumor, thus providing it with more energy and giving the tumor the ability to spread to other parts of the body (2). By utilizing a scanning technique called Dynamic Contrast-Enhanced Magnetic Resonance Imaging (DCE-MRI), these blood vessels and the surrounding tissues can be visualized in relation to their hemodynamic characteristics, such as blood flow and permeability. (2, 3) DCE-MRI works by acquiring several T1-weighted images in the same anatomical region over a short period of time while injecting a MRI contrast agent (CA). This allows for a visualization of the CA distribution within the blood vessels and the surrounding tissues. (4-6) However, the signal intensities seen on the MRI images do not correspond with the true CA concentrations in the tissues, which complicate true quantitative signal intensity values to be measured. To compensate for this, T1 relaxation maps, which are a series of MRI images with the true signal intensities of the scanned subject, are created to correct the images and provide a true quantitative measure of the signal intensities. (7-9) At The Department of Medical Physics at Aalborg University Hospital, several projects regarding DCE-MRI imaging in relation to brain cancer are being worked on (10, 11), and a technique for creating working correction maps on the department's scanner will be of value to these projects. The creation of correct maps is challenging, as different studies report different results using similar mapping techniques on similar MRI scanners (9).

In this project, a 3.0 Tesla MRI scanner affiliated with The Department of Medical Physics at Aalborg University Hospital will be used to test the usability of a mapping protocol with predetermined parameters. The mapping protocol will be compared to an Inversion Recovery (IR) technique, which is considered the golden standard for creating accurate maps (8, 9, 12, 13), but is in itself unsuited for clinical application due to unfeasibly long scan times (8). The mapping protocol will be evaluated regarding its reliability and precision compared to the IR standard, and the data will be acquired by scanning six water phantoms containing distilled water and different concentrations of CA. A software solution called Imalytics will be used to generate quantitative maps of the scanned phantoms. Imalytics is designed specifically for image handling, and is still under development. A software solution called MatLab will also be used to quantify the images and

these results will be compared with the results found in Imalytics. The results will be visualized with a relaxation time graph and Bland-Altman plots.

4.0 Background

The following section will elaborate on some of the scientific material on the subject of MRI mapping, DCE-MRI and cerebral cancer. It will also elaborate on the relevance of the project in relation to ongoing projects at The Department of Medical Physics.

4.1 Magnetic Resonance Imaging and Cerebral Cancer

MRI techniques excel in spatial resolution and visualization of soft tissue contrasts, and it is the imaging modality of choice in diagnosing and assessing certain pathological venues such as cancer, stroke and neurodegenerative disease. Cerebral cancer is one cancer type in which MRI is used in both diagnostics and assessment of treatment. (1, 14-16) Malignant cerebral tumors are one of the leading causes for cancer-related deaths in both America and Europe, with over 10 to 15 newly diagnosed cases every year per 100.000 persons (14). One such cerebral cancer form is GBM which is considered highly malignant and predominantly lethal, having a 2-year survival rate of 26.5% and a 5-year survival rate of only 5%, with a median survival of approximately 10-20 month. (1, 14-16) GBM remains a serious clinical challenge, caused by its genetic heterogeneity and the difficulties associated with assessing the effects of drugs (1). Treatment of this form of cancer is improving, but it remains one of the most fatal cancers, due in part to the tumor's ability to develop early resistance to treatments (14, 17).

The treatment of GBM can include surgery, radiation therapy and chemo therapy (18). Surgical resection of GBM is associated with an improved survival rate, and up to 65% of patients are candidates for a partial or full surgical procedure. Unlike other solid tumor types, it is impossible to remove all tumor tissue and retain life, even if the surgery is performed without consideration for the patient's neurological state after surgery. (15) Since all tumor tissue cannot be surgically removed, recurrence after surgery is unavoidable (19) and 80% of the recurrences appear within 2 cm of the site of the resection cavity (18). Studies concerning repeated resection of recurring GBM have been performed, but the evidence as to whether or not the procedure is truly beneficial remains debatable. Before both the first and second surgical resection is performed, MRI can be used to guide the procedure. MRI can be used as well to evaluate the efficacy of both surgeries. (19)

GBM is also treated with radiation therapy. MRI can be used in conjunction with PET/CT and radiation treatment planning CT for a more precise anatomical localization, which can be used to optimize delineation of the target volume. (20) MRI is also used to evaluate the effects of radiation therapy, and research suggests a strong correlation between MRI and patient prognosis (21). MRI can also be used in conjunction with stereotactic radiosurgery, where MRI scans performed before and after the procedure can be used to evaluate the efficacy of the treatment (22). MRI can also be used to distinguish radiation induced necrosis from pseudoprogression (21, 23), which is of importance as 20-30% of newly diagnosed GBM patients treated with chemotherapy and radiation therapy will experience pseudoprogression (24).

Chemotherapy is widely used when treating GBM, and an increasing amount of chemotherapies and their effects are being evaluated, accentuating the need for reliable assessment techniques such as MRI (25). There is a general consensus that the ability to noninvasively assess the effects of drugs, for example by way of DCE-MRI, is important (4). A Chemotherapeutical drug called Bevacizumab, which inhibits angiogenesis, is used when treating recurrent GBM. Angiogenesis is a process which creates new blood vessels from pre-existing ones. This process is, under non-pathological conditions, a natural part of wound healing and organ growth. (26) Angiogenesis constitutes an essential part of a tumor's malignancy, capacity for growth and metastatic ability (2, 27). When a tumor reaches a stage where its angiogenic abilities outweigh the angiogenic inhibition of the body, the tumor initiates the angiogenic process. This transition is called the "angiogenic switch", and for tumors, this is associated with a transformation into a malignant state. The vasculature created as a result of tumor angiogenesis is significantly different from vasculature generated under non-pathological conditions. (28) Bevacizumab works by inhibiting the vascular endothelial growth factor, which is a central component in angiogenesis. (26) Experiments on animal models suggest that ionizing radiation could stimulate the activity of the vascular endothelial growth factor (29).

Regardless of choice in therapeutic method, no increase in overall survival time has been observed in patients with recurrent GBM (16).

4.2 Dynamic Contrast-Enhanced Magnetic Resonance Imaging

Standard anatomical MRI techniques offer a wide variety of sequences which show the anatomical aspects of the target being scanned, but MRI also offers scanning techniques which provide insights into relevant physiological parameters. These MRI techniques are often referred to as functional or

advanced MRI. Among these advanced MRI techniques is the T1 weighted DCE-MRI scan sequence. DCE-MRI is useful for studying hemodynamics, such as blood flow and permeability, and evaluating the physiology of certain pathological conditions in cerebral cancers such as GBM (4, 21, 30). Unlike non-advanced MRI techniques, DCE-MRI can also provide enhanced insights into parameters such as cellular morphology and micro-capillary conditions. Research on cerebral cancers has provided evidence which suggests that these parameters are important in order to assess how brain tumors respond to treatment. (31) This is derived from the fact that cerebral tumors can stimulate the body to produce blood vessels through the process of angiogenesis (2, 27). The blood vessels created from tumor-initiated angiogenesis exhibit differences from normal blood vessels, which are not only anatomical, but also physiological, as vasculature generated by tumors shows increased permeability and unstable blood flow, which can result in spontaneous hemorrhaging. These abnormalities can be visualized with DCE-MRI, as they cause an increase in perfusion of the CA from the vasculature into the surrounding tissues, and the DCE-MRI technique can thus potentially have a wide use in obtaining information about tumor vascularity. (4, 30)

4.3 Magnetic Resonance Imaging mapping

The MRI mapping process allows for quantitative values to be obtained on for example T1 weighted MRI images. (7, 8, 32) As signal intensities seen on T1 weighted DCE-MRI images do not represent the absolute CA concentrations in the subject being scanned, the importance of creating T1 maps becomes evident (8). Without T1 mapping, standardization of the DCE-MRI technique is difficult, as it is influenced by individual factors such as the imaging parameters used for each scan and the concentration of signal bearing protons (7). Being able to obtain a quantitative measure of the T1 values is important when analyzing DCE-MRI images, (7, 33) and, if performed correctly, can enable a way to compare images regardless of the subject being scanned and regardless of what MRI scanner is being utilized (9). The T1 mapping process is usually performed using either an inversion recovery (IR) technique or a variable flip angle (VFA) technique (8), and for a magnetic field strength of 1.5 Teslas, both have been shown to produce sufficiently accurate T1 maps in vivo (34). The image acquisition time for IR is too long to possess any practical usability in a clinical context, but VFA scans can be performed within a few minutes (8).

4.4 Relevance

At the oncology department at Aalborg University Hospital, several scientific projects address the possibility of performing DCE-MRI scans in order to evaluate drug treatment in cerebral oncology

(10, 11), and a method to quantify their images will enable better estimations of absolute CA concentrations (7), thus improving their image analysis. Philips, in collaboration with The Department of Medical Physics at Aalborg University Hospital, is working on a software module for analysis of medical images, called Imalytics. This report will provide an evaluation of Imalytics's reliability and precision in making T1 maps, which will provide insights into the software's usability. The T1 maps generated in Imalytics will be based on the VFA technique, using predetermined flip angles of 6 and 16 degrees. The software solution is available for use at The Department of Medical Physics at Aalborg University Hospital, and an analysis of its capabilities regarding reliability and precision is important in order to verify its current usability.

5.0 Study Aim

How do T1 maps created with 6 degree and 16 degree flip angles compare in reliability and precision to inversion recovery created T1 maps on a 3.0T Philips Ingenia MRI scanner, measured in the image analysis software solution Imalytics?

6.0 Theory

This section will cover the theoretical aspects of MRI and the K^{trans} parameter. Medical MRI technology is a comprehensive field of knowledge, so this section will only present aspects relevant for the understanding of the content of this project.

6.1 Basic Principles of Magnetic Resonance Imaging

The human body contains large quantities of hydrogen atoms. These atoms are a part of chemical compounds contained in different tissues such as blood, muscle or adipose tissue. The concentration of hydrogen atoms varies between the different types of tissue, water being the substance with the highest concentration. The nucleus of the hydrogen atom, which consists of a single proton, revolves around its own axis, creating a small magnetic field around itself. This allows the proton to interact magnetically with an outside magnetic force, such as the magnetic field generated by an MRI scanner. A medical MRI scanner is characterized by a powerful static homogenous magnetic field. Modern medical MRI scanners usually have a field strength between 1.5 and 3 Teslas (35), which, in comparison, is about 60.000 times stronger than the earth's magnetic field. (36) The magnetic field on the scanner used in this project runs in the longitudinal direction, meaning that when a person is placed in the scanner head first, the magnetic field will run in the direction of the

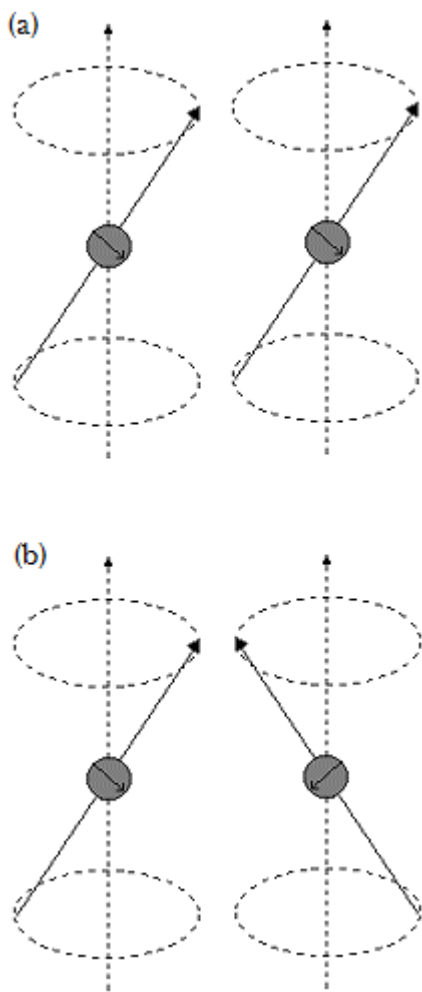


Figure 1: (a) protons spinning in phase (b) protons spinning out of phase

length of the person's body. This direction is also referred to as the z-axis, or the longitudinal axis. When the hydrogen protons are within the MRI magnetic field, their axes will align themselves in a parallel or antiparallel direction in relation to the static magnetic field. This is called longitudinal magnetization. The ratio of the parallel and antiparallel protons is related to the strength of the magnetic field. The number of parallel protons is always higher than the number of antiparallel protons, and this ratio increases with increasing magnetic field strength. Therefore, higher field strengths will result in proportionally more protons aligning in the parallel direction. This also means that higher field strength increases the net magnetization vector, which is the difference in magnetic strength between the parallel and antiparallel protons. The protons spin around the magnetic field's directional axis at an angle, called precession. The rate by which they complete a rotation around the axis happens at a certain frequency, called the Larmor frequency. When the protons spin identically, they are referred to as being in phase, and when they do not, they are out of phase. See figure 1 for the difference between in phase

and out of phase. The Larmor frequency of the hydrogen protons is dependent on the strength of the magnetic field they are subjected to. The higher the strength of the magnetic field, the higher the Larmor frequency will be. The MRI scanner uses radio frequency (RF) pulses with a similar frequency as the protons' Larmor frequency. This RF pulse forces the axes of the protons to turn for example 90 degrees, pushing the protons out of the longitudinal plane and into the transverse plane, resulting in the protons becoming perpendicularly aligned in relation to the scanner's magnetic field. This RF pulse also causes the protons to spin in phase. From the transverse plane, the protons will gradually fall out of phase and their axes will return to the longitudinal plane. (35)

The scanner also contains gradient coils. A gradient coil is a device containing several loops of wire, which are used to produce gradual and intentional field strength variances in the homogenous magnetic field. These variances create differences in the Larmor frequency of the protons, depending on their location in relation to the now inhomogeneous magnetic field, allowing for

spatial differentiation between the protons. There are three gradient coils in a MRI scanner, one for each of the x, y and z axes. The gradient coils, in collaboration with the RF pulses, will fill out K-space during a scan, and thus create the MRI image. K-space is a matrix of points in which the signals from the protons are stored and transformed, via Fourier transformation, into the MRI image. (35, 37)

6.2 T1 and T2 Relaxation

As mentioned above, the spinning protons align in either a parallel or antiparallel direction in relation to the MRI scanner's magnetic field. Protons with their axes parallel with the MRI scanner's magnetic field are defined as being in a low energy state, whereas protons aligned in the antiparallel direction are defined as being in the high energy state. The ratio of protons in the low energy state versus the high energy state will increase with increasing external magnetic field strength. Therefore, a 3.0T scanner will have proportionally more protons in the low energy state compared to the high energy state, than for example a 1.5T scanner. When for example a 90 degree RF pulse is introduced, the spinning axes of the excess protons shift 90 degrees from the longitudinal z-axis into the transverse x,y-plane, see figure 2.

Once in the transverse plane, their axes will begin to turn back towards their original longitudinal state. The time it takes 63% of the protons to revert back to the longitudinal magnetic field is called the T1 relaxation time, and it is achieved by the release of energy from the protons into the surrounding tissue. This release of energy happens at the Larmor

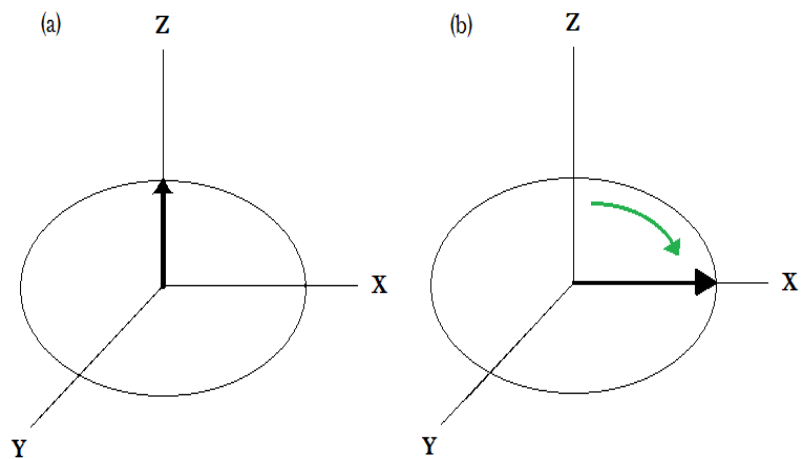


Figure 2: (a) Before the 90 degree pulse, the excess protons are aligned with the z-axis. (b) After the 90 degree RF pulse, the axes of the protons shift into the x,y-plane

frequency and the signal this process creates can therefore be registered and imaged by the scanner. The duration of this process varies between the different tissue types. For example, soft tissue has a short relaxation time compared to aqueous tissues. In general, tissues made of larger molecules have shorter T1 relaxation times than tissues made of smaller molecules. Therefore, the intensity of the T1 signal is related to the molecular structure of the tissue types, where the liquids will appear

relatively dark because of their slow relaxation times, and solid tissue types will appear relatively bright. (35)

Apart from the T1 signal, there is also a T2 signal. Where the T1 signal is derived from the release of energy into the surrounding tissues when the protons realign themselves with the external magnetic field, the T2 signal relates to the phase decay of the spinning protons. (35, 37) This decay is caused by two different factors: spin-spin interaction and decay caused by inhomogeneities in the external magnetic field. The spin-spin dephasing is the result of the individual magnetic fields of the spinning protons interaction with each other. Inhomogeneities in the external magnetic field cause protons in different locations to be exposed to different magnetic field strengths. As a result, the protons precess at slightly different frequencies, which cause T2 dephasing. (37) The variations caused by the external magnetic field can be minimized with a coil type called shimming coils, though not completely eliminated (38, 39). Spin-spin interaction is dependent on the proximity of the protons to each other. If the protons are close, as in solid tissue, this dephasing effect is more prominent. (37) As shown on figure 1, protons can be both in phase and out of phase. When a 90 degree RF pulse is introduced, the protons will flip into the x,y-plane and go into phase with each other. When the RF pulse stops, the protons will gradually go out of phase again. This relaxation process is much faster than the T1 relaxation process for the same tissue type. The different rates of proton decay cause their axes

to fan out as seen in figure 3. When a 180 degree pulse is used to invert the spins, the individual dephasing protons reverse their direction, but maintain their individual speed, which means the process is reversed and they return to phase. (35, 37)

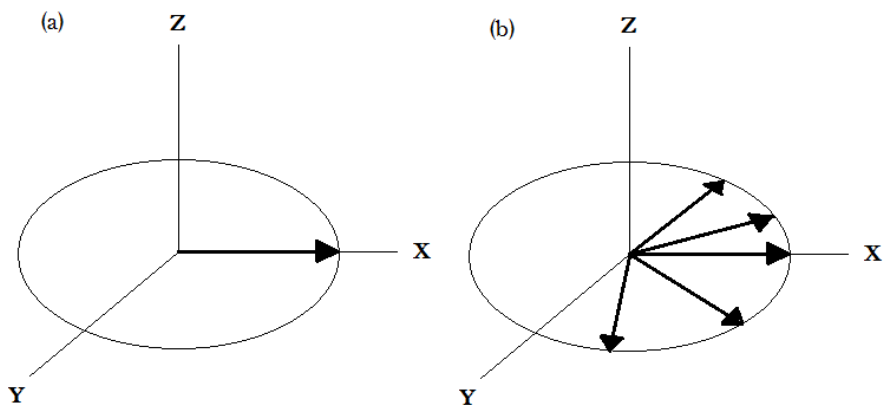


Figure 3: (a) protons are in phase in the x,y-plane. (b) protons dephasing at different speeds, causing them to fan out.

6.3 Contrast Agents

A large variety of MRI CAs exist, and they can vary greatly in their chemical composition. A subtype of CAs is the paramagnetic agents, which consist of a metal ion with one or more unpaired electrons. Gadolinium-based CAs, such as Dotarem, falls into this subtype of CAs. When Dotarem

is added to water, magnetic interaction between the magnetic moments of the water molecules and the gadolinium molecules causes a reduction in relaxation times. CAs are either T1 specific or T2 specific, depending on which type of relaxation they exert a greater influence on. T1 specific CAs can be used as T2 CAs as well, depending on, among others, the MRI scan sequence and the magnetic field strength. (40) Dotarem is a T1 specific CA, as it has a greater sensitivity in T1 weighted MRI images (41). It is secreted primarily through the kidneys (40, 42), with about half of the CA being secreted after 80 minutes. Due to the metabolic differences between normal tissue and tumor tissue, a much higher uptake of CA can be seen in tumorous tissues on MRI images. (40) The CA is distributed through the vascular system and leaks, depending on the vascular permeability and the blood flow, into the surrounding tissues and extracellular extravascular space (EES). (43) Under non-pathological conditions, CA is prevented from passing through the blood brain barrier. In certain pathological conditions, including cancerous tumors, the permeability of the cerebral capillaries change, allowing the CA to pass beyond the blood brain barrier. (40, 44)

CAs can be used when performing a variety of MRI scans, including DCE-MRI of patients with GBM, where the CA is administered by intravenous injection. (5, 8, 45) The signal intensities on the T1 DCE-MRI images do, however, not correspond with the contrast concentration in the tissues, which accentuates the importance of relaxation maps. These maps work as an adjustment to the signal intensity values on the MRI images, making these intensities correspond with the actual contrast concentration in the tissues (7), allowing for the measurement of parametric values such as K^{trans} . (46)

6.4 T1 Maps

T1 relaxation maps are used to determine the true T1 relaxation times in images on a pixel-by-pixel basis (8, 32). The standard way to determine T1 maps, are by way of the spin echo inversion recovery technique or variable flip angles. T1 maps are used to adjust MRI images in order to show the true proportionality between MRI signal intensity and CA concentration. The T1 mapping process is considered a possible way to improve diagnostic accuracy (8), and is used in characterization of tissues present in the cerebrum (32). When creating maps in a practical setting, the scan sequences needed to create the map are executed before injection of CA.

6.4.1 Inversion Recovery Technique

This type of MRI technique can be executed in a number of different ways, but the golden standard when computing T1 relaxation times in vitro is the spin echo inversion recovery technique (8, 9, 12,

13). It is used as the conventional method, as it is not affected by inhomogeneities in the external magnetic field. This technique can be conducted by repeating a certain sequence of RF pulses, and by defining a number of parameters: time of repetition (TR), time of inversion (TI) and time of echo (TE), see figure 4.

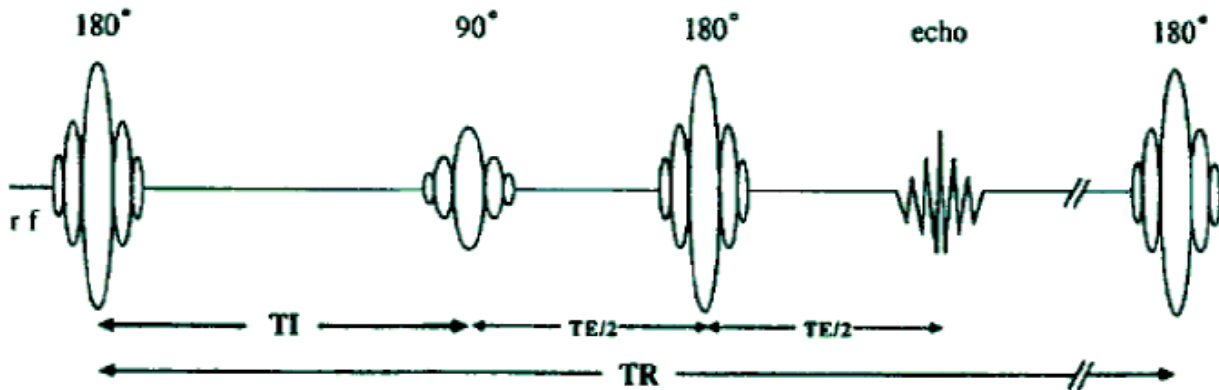


Figure 4: An inversion recovery sequence showing TI, TR, TE/2 and the 90 and 180 degree RF pulses.

As seen in figure 4, TR is the total time it takes to complete one sequence, TI is the delay between the initial 180 degree RF pulse and the 90 degree TI RF pulse, and TE is the time from the TI RF pulse and the time of echo, where the signal is sampled. At TE/2, another 180 degree RF pulse is executed to refocus the echo and form the signal. The last 180 RF pulse in the sequence is executed at TE/2 and reverses the T2 dephasing process caused by the spin-spin relaxation and external magnetic inhomogeneities. (8) The gradient coils are used to ensure that the T2 decay remains in a dephased state thus suppressing the T2 signal from the T1 mapping image (47, 48). The sequence is time consuming, as the TR must be at least five times the T1 time of the longest T1 relaxation time of the scanned matter. The long TR ensures that ~99% of the protons have returned to their equilibrium as either parallel or antiparallel to the external magnetic field. The sequence is repeated at least 5-6 times with different TI values, as this produces multiple T1 time/intensity points. These points are then plotted into a schematic, to produce a curve from which the T1 relaxation time can be computed. To produce a complete T1 map, generating such a schematic on a pixel-by-pixel basis will enable calculation of the correct T1 relaxation time for each particular pixel. (8)

6.4.2 Variable Flip Angle Technique

As well as inversion recovery, VFA technique can be used to generate T1 maps for the quantification of MRI images. This method does not suffer from the long scan time issues associated with inversion recovery, and is therefore, in that regard, more applicable in clinical

situations. (8) Because of its short scan time, VFA is also very well suited for use in combination with DCE-MRI (49). The VFA method uses two or more different flip angles to accurately determine the T1 relaxation times. The process involves RF pulses which usually produce flipping angles lower than 90 degrees. (8) This allows for very short TR times. If a 90 degree RF pulse was used with the same very short TR time, it would not give the longitudinal recovery process time enough to produce a reasonable signal. The VFA technique does not utilize the refocusing 180 degree RF pulse, as seen with IR, as this would require a longer TR time to acquire the signal, and thus defeat the purpose of the VFA technique. (50) The magnetic homogeneity of the RF pulse is an important aspect when using the VFA method (51, 52), and with higher field strengths comes a larger degree of inhomogeneity in the RF pulse (52).

6.5 Dynamic Contrast-Enhanced Magnetic Resonance Imaging

When acquiring DCE images, the same anatomical region is visualized rapidly and repeatedly over time after the injection of CA. This provides insights into the distribution of the CA through the vascular system and surrounding tissues within a certain frame of time. The DCE-MRI images visualize the differences in microvascular permeability, blood flow and vessel size in the selected anatomical region. (4-6) DCE-MRI is used in the diagnostic process for a wide variety of pathological conditions such as ischemia, stroke and cerebral cancer (4, 53).

6.6 The K^{trans} Parameter

DCE-MRI allows for an evaluation of hemodynamic parameters of interest. One of these parameters is the amount of fluid passing from the vasculature to the EES during a predefined amount of time. This parameter is referred to as K^{trans} , or the transfer constant. K^{trans} is dependent on two factors: The permeability of the vasculature and the surface area product of the vasculature. These two factors can affect the K^{trans} value, as a high permeability will allow for more fluid to cross over into the EES, and a large surface area of the vasculature will increase the amount of fluid which permeates into the EES within the same time period. This value can be used to detect pathological perfusion abnormalities within organs such as the brain. (46)

7.0 Method

In this section the design to acquire the data for T1 mapping and the software to analyze it will be explained, as well as the statistical analysis methods used for calculating the results. The focus for the design of the data gathering process and the analysis of data is to enable a comparison between the T1 maps generated in Imalytics with the predetermined flip angles and the T1 maps generated in MatLab using the golden standard IR technique. This will enable a comparison between the results found with Imalytics and those found with MatLab regarding reliability and precision in creating correct T1 maps. For an over view of the data handling process, see appendix 1, and for the literature search see appendix 2.

7.1 Study Design

For the collection of data, six phantoms were created using 1,5L plastic bottles (Picture 1), each containing 1,57L of liquid, prepared with distilled water containing different concentrations of Dotarem MRI CA. The concentrations for each phantom can be seen in table 1. As can be seen in



Picture 1: The six water phantoms.

table 1, the concentrations are not even numbers, even though this was originally intended. A modification was made, as a small test revealed that the phantoms did not contain 1,5L of liquid, but 1,57L. This issue was corrected by weighing an empty bottle and a full bottle, deducting the weight of the empty bottle from the full bottle and, under the assumption that 1 centiliter of distilled water weighs 1 gram, calculating the

Bottles (1,57 L)	Dotarem (ml)	Conc. (mmol/L)
1	0	0
2	0,6	0,191
3	1,8	0,573
4	3	0,955
5	6	1,911
6	9	2,866

Table 1: Table showing the phantoms, the amount of Dotarem added and the concentrations.

modified concentrations based on 1,57L of water in the bottles. All scans were conducted with a Philips Ingenua 3.0T MRI scanner using a dStream HeadSpine coil. For the VFA images, the matrix size was 160 X 128, and the voxel size 2,5mm X 2,5mm X 2,5mm. For the IR images, the matrix size was 64 X 42, and the voxel size was 1,88mm X 2,5mm X 5mm.

The phantoms were placed in the coil as seen in picture 2. All phantoms were individually scanned a total number of three times. The scanning protocol used for each scan contained twelve IR series and two VFA series. For an overview of the TI inversion recovery times used, see appendix 3. For

the IR series, a TR = 15000ms was used, and a TE = 5,2ms. For the VFA series, a TR = 50ms and a TE = 1,7ms was used. The VFAs used in this study were set at 6 and 16 degrees, with a TR = 50ms and a TE = 1,7ms. The IR series are based on Zhou’s work (8), supported by other scientific publications (9, 54). Under optimal conditions for accurate T1 estimation using VFAs, adjustments for the inhomogeneities in the RF field would be incorporated in the scan protocol and data analysis. RF field inhomogeneities arise due to the presence of an object within the scan field (8). However, it was not possible to obtain this information from the scanner with the current software access levels available to the staff. The scanner did, however, perform a RF calibration scan before any VFA or IR series were executed.



Picture 2: Placement of the phantom within the coil.

7.2 Magnetic Resonance Imaging Contrast Agent

As mentioned above, the contrast agent used for this experiment was Dotarem (generic name: gadoterate meglumine), which is a gadolinium-based substance. It was approved by the FDA on the 20th of March 2013 (55) and has a concentration of 0,5mmol/mL (41).

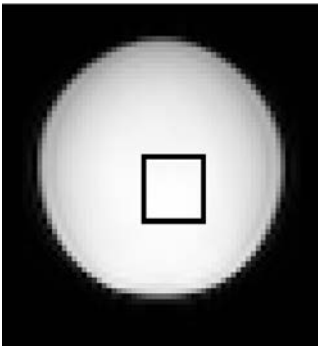
7.3 MatLab Processes

For this report, the MatLab software was used to determine the reference IR T1 relaxation times and generate the relaxation time graph and Bland-Altman plots used for evaluating and visualizing the reliability and precision of the Imalytics software. The MatLab software was chosen, since it is able to identify the IR T1 relaxation value for water, based on the reference T1 relaxation time for cerebral spinal fluid (CSF) obtained from the software of the 3.0T scanner used in this report, see table 2. The CSF value was used, as the T1 relaxation time for water and CSF is the same (56).

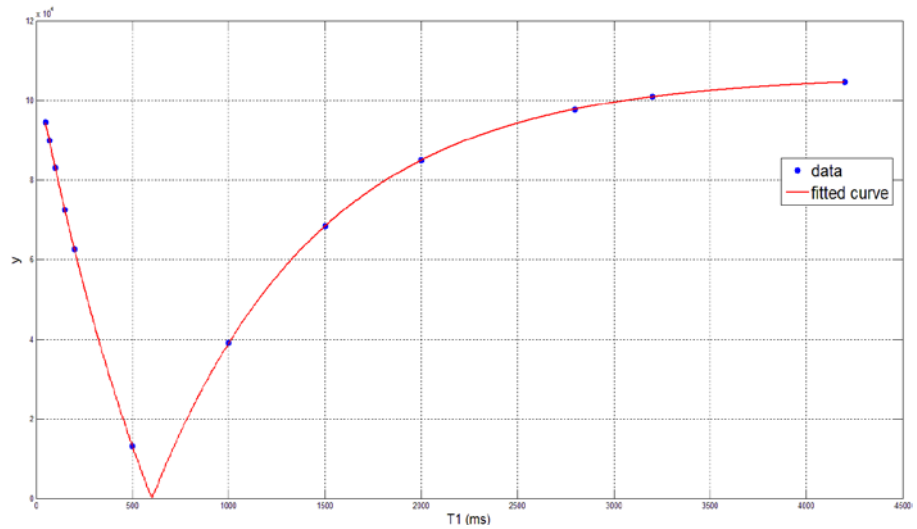
Tissue	on 1.0T systems			on 1.5T systems			on 3.0T systems		
	T1 [ms]	T2 [ms]	Rho [%]	T1 [ms]	T2 [ms]	Rho [%]	T1 [ms]	T2 [ms]	Rho [%]
Grey matter	772	100	85	920	100	85	1200	100	85
White matter	650	90	70	780	90	70	1010	90	70
CSF	2100	160	100	2400	160	100	3120	160	100
Skeletal muscle	710	45	70	870	45	70	1161	45	70

Table 2: T1 relaxation time for Cerebral spinal fluid for a MRI scanner with an external field strength of 3.0T (red box).

The MatLab accessory tool Curve Fitting Toolbox version 3.4 was used to calculate the T1 relaxation times from the IR image series on each of the three data sets obtained for each of the six phantoms. The T1 relaxation times for IR were used to compare with the VFA relaxation times measured in Imalytics. For the IR series, this was done by rescaling the MRI images and placing a square Region of Interest (ROI) in the center of the image, measuring 10x10 pixels, as seen in picture 3, for each of the twelve TI times in order to generate a curve as seen in graph 1. In total, eighteen curves were generated, one for each of the six phantoms scanned on three separate days. See appendix 4 for the script used to rescale the images and create the ROI.



Picture 3: IR image in MatLab with a 10x10 pixel ROI (black box).



Graph 1: Example of a fitted Inversion Recovery curve based on twelve IR scans performed on a single phantom, visualized in MatLab. Each of the blue points represents a T1 relaxation time for each of the twelve TI times. The X-axis represents the TI time, and the Y-axis represents the signal intensity. The T1 relaxation time for the phantom being scanned is equal to the point where the fitted curve intercepts the X-axis.

The ROI defines the area where the mean signal intensity is measured, based on the signal intensity in each pixel within the ROI. The fitted curve was created using the following equation:

$$S = \left| S_0 * (1 - (1 - \cos(\theta))e^{-\frac{TI}{T1}}) \right|, \quad (\text{eq. 1})$$

where S equals the signal intensity, S₀ is the steady state signal intensity, T1 equals the estimated T1 and θ is the angle of the initiation pulse. Steady state in this case refers to a longitudinal magnetic equilibrium which is present right before an excitation pulse. This equilibrium is achieved when the amount of magnetization flipped into the x,y-plane equals the recovered amount of magnetization on the longitudinal axis during TR, which occurs after a number of excitation pulses.

(57) Eq. 1 was created and adapted from the equations used in (54) and (58), which can be seen below.

$$S = \left| S_0(1 - (1 - \cos(\theta))^{-TI/T_1}) \right|, \quad (\text{eq. 2}) \quad (54)$$

where S equals the signal intensity at TI, S_0 equals the steady state signal intensity and θ is the inversion pulse angle (54). It should be noted, that equation 2, taken from (54), is flawed, as an e is missing. The e was added to the MatLab equation by the MRI physicist from the Department of Medical Physics, based on equation 3.

$$M_z(t) = M_0 \left[1 - (1 - \cos \theta_{inv}) e^{-t/T_1} \right], \quad (\text{eq. 3}) \quad (58)$$

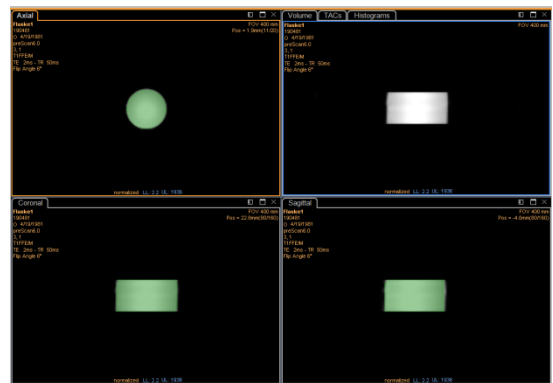
where $M_z(t)$ is the time-dependent longitudinal magnetization, t is the elapsed time period and θ_{inv} is the angle of the inversion pulse (47). The confidence intervals for the IR curve fits, as supplied by MatLab, can be seen in appendix 5.

7.4 Ianalytics

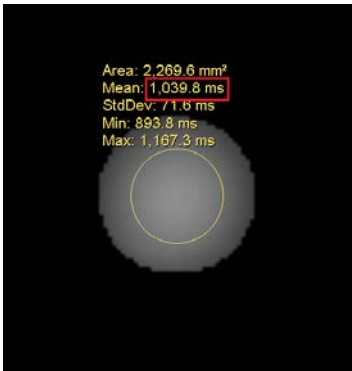
This software is under development by Philips for the purpose of analyzing a wide variety of medical images in relation to a number of functions, including quantitative analysis of MRI images (59). For the purposes of this report, Ianalytics was used to create T1 relaxation maps based on the 6 degree and 16 degree VFA scans. These were then compared to the T1 relaxation times for IR calculated in MatLab.

Creating relaxation maps in Ianalytics is a process involving several steps. The first step consisted of

importing the VFA images from the phantoms to the software. Then all VFA images were rescaled. This rescaling process was necessary in order to enable to software to generate correct maps. Next, a Volume of Interest (VOI) was automatically created on the 6 degree VFA scan. This process consists of a green delineation of the entire phantom, as seen on picture 4. Since the physical proportions of the phantom on each of the two VFA scans are identical, the same VOI was used on both scans. The software then used the signal intensities measured within the VOIs on the VFA scans to create a T1 relaxation map. The finished T1 relaxation map consisted of 20 images



Picture 4: The automatic VOI created by the Ianalytics software on the MRI images. The green colour represents the delineated area.



Picture 5: The ROI (yellow circle) placement on the T1 map. The mean signal intensity (red box) represents the true T1 relaxation time as calculated by Imalytics.

showing the phantom with its absolute signal intensity. Three T1 relaxation maps were created for each phantom, one for each scan session, creating a total of eighteen maps. After the maps were created, the absolute T1 relaxation times were measured by placing a circular ROI in the center of the phantom on the 11th slice in the image series and noting the mean signal intensity measured within the ROI. See picture 5 for a view of the placement of the ROI. The 11th slice was chosen, as it corresponds with the same position within the phantom where the IR scans were performed.

As the Imalytics software is not yet fully developed, it is important to note that it is for research purposes only (59).

7.5 Statistical Analysis

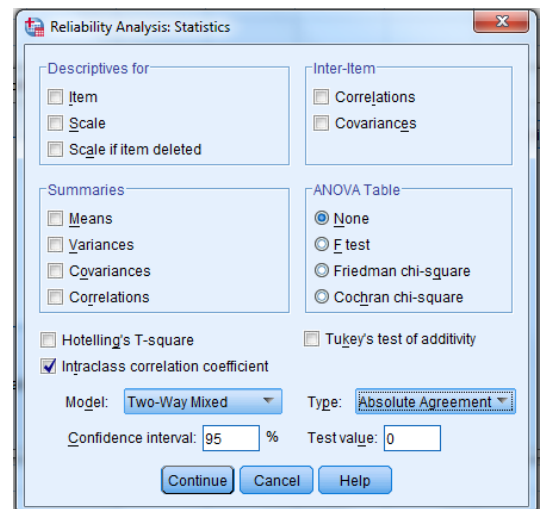
To evaluate the results found in Imalytics and MatLab, and compare them with each other, a relaxation time graph and Bland-Altman plots were generated, as well as Coefficients of Variation (CV) for precision and Intraclass Correlation Coefficients (ICC) for reliability. SPSS was used for the ICC calculations and MatLab was used for the graph Bland-Altman plots, see appendix 6 and 7 for the MatLab scripts.

The CV and ICC values for this report were based on the data seen in appendix 8. Each of the two methods generated six CVs, one for each phantom, which was processed into a single mean CV for each method. The ICCs will be done by comparing the day-to-day variances in the T1 relaxation times for the six phantoms.

7.5.1 Intraclass Correlation Coefficient

This type of test was chosen, as it is considered a useful tool in the assessment of reliability, and can be used when a test is repeated more than once (60, 61). The reliability was determined by calculating one ICC for each method. The data represented the T1 relaxation times measured in Imalytics and MatLab, based on the VFA and IR scans done on each of the three days, and on each of the six phantoms.

The settings used in SPSS were as follows. In the



Picture 6: Screenshot from SPSS showing the settings in the "Statistics" tab.

“Analyze” menu, under “Scale”, the test type “Reliability analysis” was selected. The settings in the “Statistics” tab can be seen in picture 6.

Within the “Statistics” tab, the Model “Two-Way Mixed” and the Type “Absolute Agreement” were chosen. The “Two-Way Mixed” setting is used when an identical test is performed several times on the same subjects and the differences between the tests are of interest (60). In the case of this data set, the six phantoms were scanned with an identical protocol on all three different days, and any day-to-day variance in the measured T1 relaxation maps are of

Day_1_VFA	Day_2_VFA	Day_3_VFA
9579,00	3477,00	4598,00
914,00	1048,00	1021,00
465,00	470,00	458,00
204,00	198,00	207,00
72,00	71,00	78,00
30,00	31,00	31,00

Table 3: Data sheet from SPSS showing the data points used in the ICC analysis for the VFA method.

interest. The Type setting “Absolute Agreement” considers any systematic differences between the different tests (60), and takes the test-to-test variances into account (62). In relation to this report, this setting will take any systematic differences, which exist between the day-to-day scans into consideration. The data points used consisted of the T1 relaxation measurements for each method, IR MatLab and VFA Imalytics, and for each of the six phantoms, giving a 3 x 6 data matrix as seen in table 3, with the VFA data set as example. The ICC value is set by some publications to range from -1 to 1, where a -1 represents perfect disagreement and 1 represents perfect agreement, although it is debatable whether a negative ICC is theoretically possible in a two-way intraclass correlation analysis (63).

7.5.2 Coefficient of Variation

The CV method has the assumption of normal distribution of the data. To test this assumption, a normality test was performed in SPSS, which can be seen in appendix 9. The results from this test confirm the assumption that the data has normal distributions. The CVs were calculated using the following equation:

$$CV = \frac{SD}{\bar{X}} * 100\% , \tag{eq. 4} \tag{64}$$

where SD is the standard deviation and \bar{X} is the mean value of the data. The standard deviation is given by the following equation:

$$SD = \sqrt{\frac{\sum X_i^2 - \frac{(\sum X_i)^2}{n}}{n-1}} , \tag{eq. 5} \tag{64}$$

where X_i are the individual T1 relaxation times and n is the total number of measurements. The set of X -values varied, depending on the phantom and which of the IR or VFA methods the data points would be relevant for. For example, for the calculation of the CV for the second phantom, regarding the VFA method, the X -values were 914, 1048 and 1021, as seen in appendix 8 and in picture 7. The final CV results for the IR and VFA methods will be given by a mean CV value for each method.

7.5.3 Bland-Altman Plots

The Bland-Altman plot created for this report is a residual regression plot. In order to make the plot, the data points the regression line was created from were made by plotting the data as the mean of the two data points (X-axis) vs. the difference between the same two data points (Y-axis). The two data points used to calculate each plot point were the VFA and IR values for a specific phantom and a specific scan date. The resulting scatterplot was used to draw the regression line. The residual regression plot could then be created by creating a new scatterplot where the data points consisted of coordinates based on the residual values of the previous data points in relation to the regression line. Limits of agreement are added to the plot which are given by:

$$\pm \text{mean} + 1.96 * \sqrt{\pi/2} \text{ SD} \quad \Rightarrow \quad \pm \text{mean} + 2.46 \text{ SD} \quad (\text{Eq. 6})(65)$$

7.5.4 Relaxation Time Graph

The graph plot seen in graph 2 was made by plotting each VFA relaxation time with the mean IR value for each phantom, resulting in three points for each phantom, distributed along the x-axis according to the mean IR value. The graph also features an identity line, which resembles the measured IR values, and serves as a reference.

8.0 Results

In this section, the results of the statistical analyses regarding the CV and ICC for the VFA and IR methods will be presented, as well as the Bland-Altman plots and the relaxation time graph. The ICC and CV calculations were based on the raw data seen in appendix 8, and the results of the analyses can be seen in table 4. Additional ICC and CV analyses were made in order to enable an evaluation of a suspected outlier in the VFA data. The results of the additional analyses can be seen in tables 5 and 6.

8.1 Intraclass Correlation Coefficient and Coefficient of Variation

Table 4 presents the main results of the report. The ICC values are listed with their confidence intervals in brackets.

CV(%)		ICC	
IR (MatLab) (ms)	FA 6/16 (Imalytics) (ms)	IR (MatLab) (ms)	FA 6/16 (Imalytics) (ms)
0,821071998	12,15015804	1 (CI = 1/1)	0,723 (CI = 0,266/0,950)

Table 4: Overview of the main results. The listed CV values for the IR and VFA methods were calculated from the individual CV values from each of the six phantoms. The ICC results are listed for both IR and VFA as well, with their respective confidence intervals.

8.2 Additional Analyses

For the additional ICC analysis, the data were generated by excluding the VFA data point from phantom one with a T1 relaxation time of 9579ms, as seen in appendix 8, as it is a possible outlier. The result can be seen in table 5.

	Intraclass Correlation ^b	95% Confidence Interval	
		Lower Bound	Upper Bound
Single Measures	,994 ^a	,968	,999
Average Measures	,998 ^c	,989	1,000

Table 5: Screenshot from SPSS showing the result for the additional ICC analysis performed without the suspected outlier. The ICC for Single Measures is highlighted, as well as the confidence intervals.

For the additional CV analysis, a mean CV value was calculated by excluding the CV value for phantom one. The result of this calculation, as well as the original calculation with all data points included, can be seen in table 6.

Phantoms:	CV(%) (All data)		CV(%) (Possible outlier removed)	
	IR (MatLab) (ms)	FA 6/16 (Imalytics) (ms)	IR (MatLab) (ms)	FA 6/16 (Imalytics) (ms)
1	0,643735112	55,19620074	0,643735112	19,63261181
2	1,072269234	7,127229904	1,072269234	7,127229904
3	0,848143489	1,29814367	0,848143489	1,29814367
4	0,384793292	2,257426451	0,384793292	2,257426451
5	1,001334721	5,139283571	1,001334721	5,139283571
6	0,97615614	1,882663921	0,97615614	1,882663921
Mean	0,821071998	12,15015804	0,821071998	6,223

Table 6: The CV values for all the phantoms for both the IR and VFA method. The original CV calculations are shown next to the calculations performed after excluding the possible outlier from phantom one with the VFA method. The bottom row shows the means for each column.

8.2 Bland-Altman Plots

Two Bland-Altman plots were made. The first plot, seen in figure 5, shows a Bland-Altman plot where the data points are defined as having an x-coordinate which is the average T1 relaxation values of the IR and VFA data, and a Y-coordinate which is the VFA value minus the IR value. On the plot in figure 5, a regression line has been added, as well as limits of agreement, seen as 95% confidence intervals. These are used to generate the residual regression Bland-Altman plot seen in figure 6, which is generated by flipping the regression mean line seen in figure 5 down, so that it becomes the mean line seen in figure 6. All the data points in figure 6 are adjusted accordingly so as to represent the residuals.

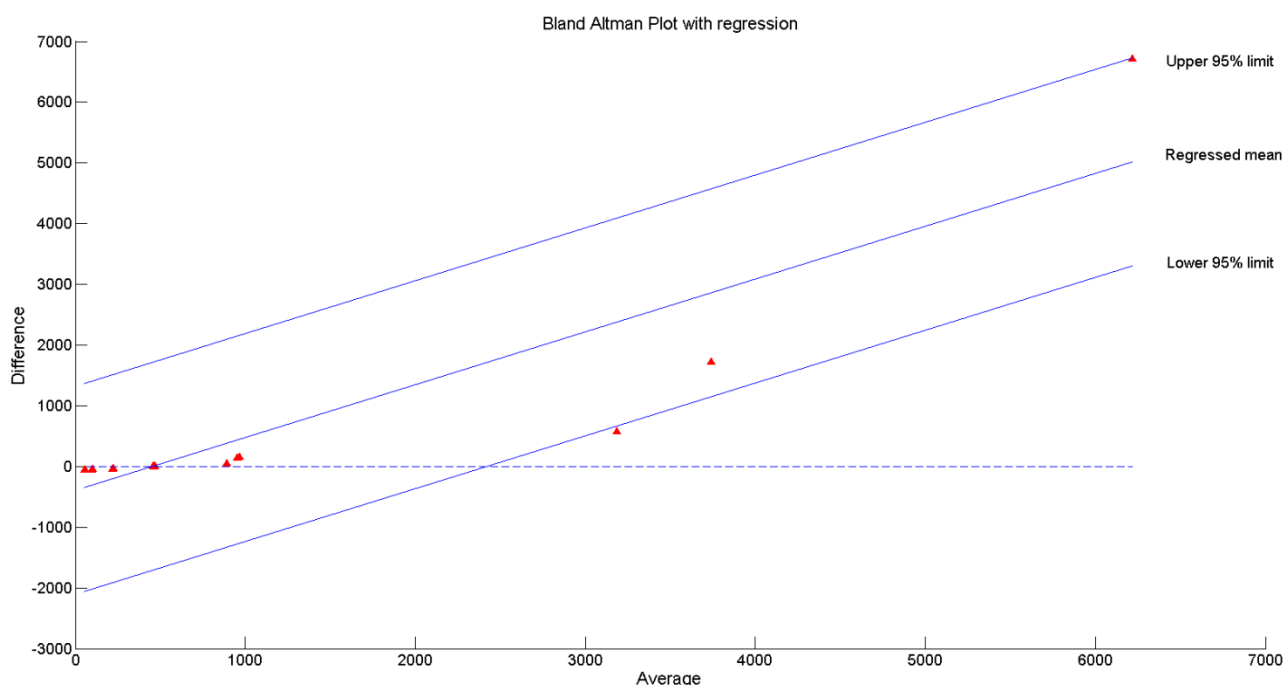


Figure 5: Bland-Altman plot showing the data points from the IR and VFA raw data, plotted as their average T1 relaxation values on the X-axis and their differences on the Y-axis. The regression line can be seen as well, with the 95% confidence interval.

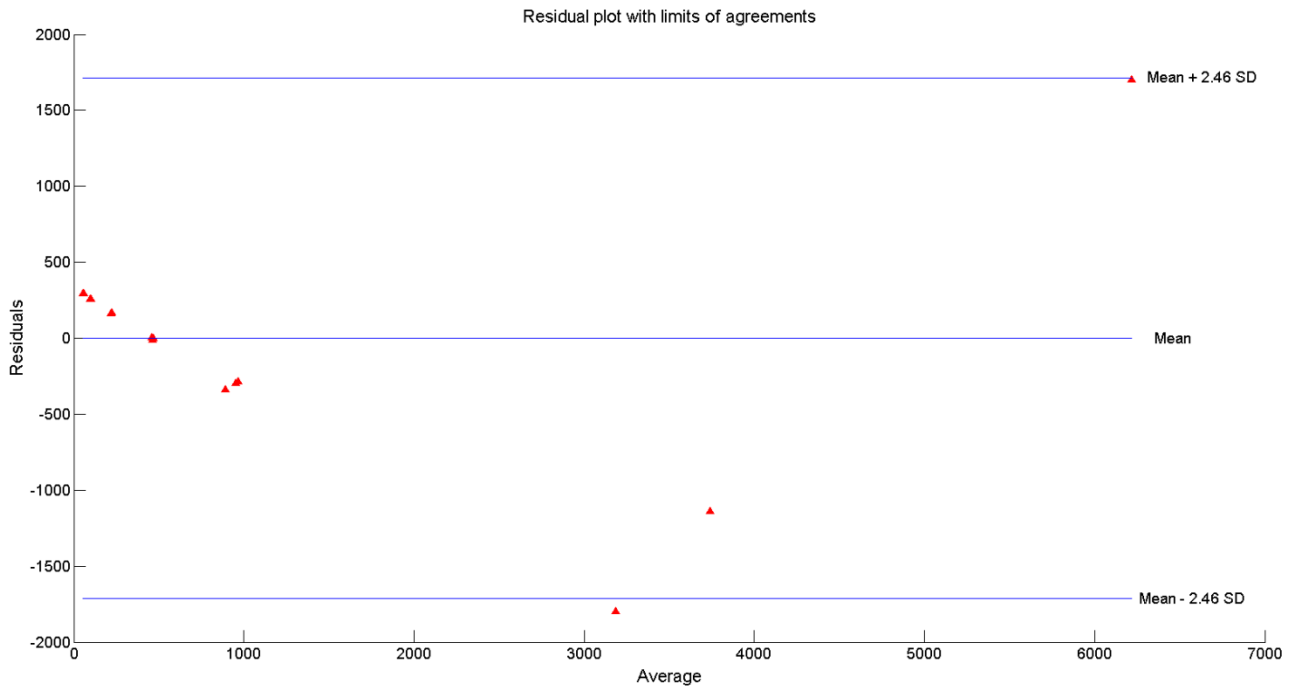
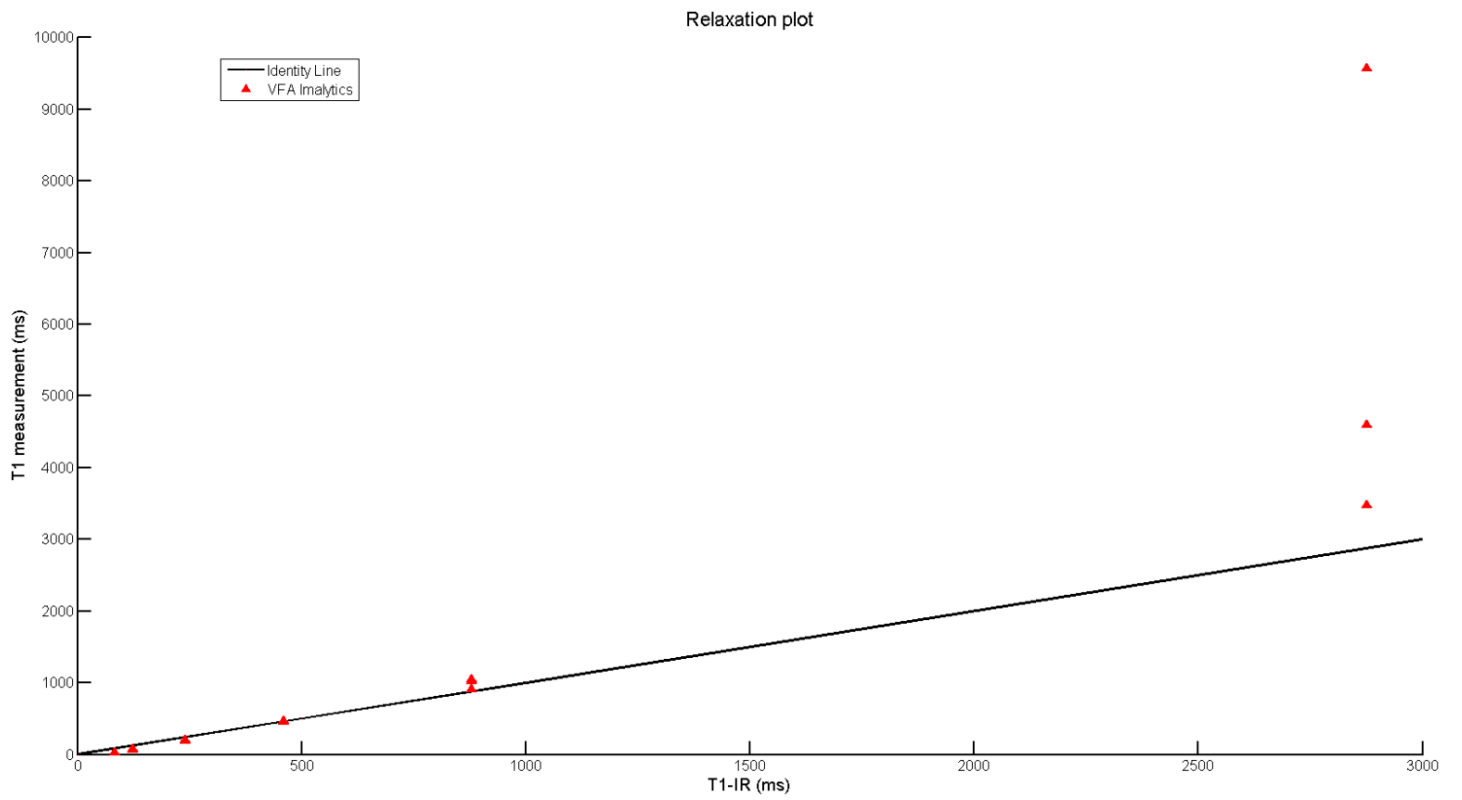


Figure 6: The residual regression Bland-Altman plot, showing the data points (red triangles), the mean regression line and the limits of agreement.

8.3 Relaxation Time Graph



Graph 2: The T1 relaxation time graph for the VFA method. The black line represents the identity line, created by plotting a line through the mean IR relaxation times for each phantom. The red triangles represent the VFA data points. The IR T1 relaxation measurements are represented on the X-axis, and the T1 relaxation times for the VFA data points are on the Y-axis.

9.0 Discussion

In this section of the report, the results and the method will be discussed. Based on the findings for the IR and VFA methods, with an ICC = 1 and a CV = 0.82% for IR and an ICC = 0.723 and a CV = 12.15% for VFA, the discussion will address the possible outlier and its impact on the final results, as well as a comparison of the results in relation to other scientific publications. The part of the discussion regarding the method will address alternative scanning methods as well as the Imalytics software.

9.1 Possible Outlier Evaluation

In the data set seen in appendix 8, a single VFA data point stands out as a possible outlier, with a measured T1 relaxation time of 9579ms compared to a mean of 4038ms (SD = 793ms) for the two other measurements on the same phantom with the VFA method. The distance to that mean for this possible outlier is almost seven SDs. This raises suspicion, as all of the other data points for the VFA method across the other five phantoms are within two SDs of their respective means. This data point was, however, included in the analysis, as it was not possible to identify the cause behind the unusually high value, and thus did not exhibit an obvious reason to be an outlier. Deleting possible outliers from a data set is a controversial issue and can be viewed as inappropriate, and should not be done unless it can be established with certainty that the data point is truly an outlier (66).

9.2 Coefficient of Variation

There is no doubt that the possible outlier has had a measurable effect on the mean CV for the VFA method, as the CV value for phantom one is 55.2%, and the CV for all other phantoms are below 10%, as seen in table 6. The CV value for phantom one causes the mean CV to rise to 12.15%. If a CV of 10% or less is considered acceptable (61), then this possible outlier may cause the mean CV of the VFA method to appear less acceptable. If the possible outlier is excluded, and the mean CV for VFA is recalculated, the CV becomes 6.22%, as seen in table 6. If the same limit for acceptance of 10% is used (61), then the exclusion of the possible outlier causes the CV result of the experiment to become acceptable.

The correct interpretation of the CV values might, in the case of the results found in this report, be imprecise, as the CV method assumes heteroscedasticity in the data set (61). Heteroscedasticity is a phenomenon where the largest measurements have the largest variances in relation to the variance for lower value measurements (61). For the data set used in this report, it can be challenging to truly

determine whether the data fulfills the assumption of heteroscedasticity, as all measurements from all phantoms except phantom one lie closely together, as seen on graph 2 in the results section. However, since no outliers can be identified with certainty, and all data points were therefore included in the analysis, heteroscedasticity can be assumed. Also, looking at the data for VFA in appendix 8, heteroscedasticity might be assumed, as there is a tendency for the larger data values to deviate more than the lower values. An example of the low deviation in the lower values with the VFA method can be found for phantom six, which has measured T1 relaxation values of 30, 31 and 31. An example of the somewhat higher deviation in values for the VFA method can be seen for phantom two, with the measured values 914, 1048 and 1021. One could speculate, based on the aforementioned values, that the measurements for phantom two would have a higher variance than the measurements for phantom six, thus confirming a possible heteroscedastic tendency. The pattern of distribution of data points seen in the residual Bland-Altman plot would also suggest heteroscedasticity (67).

9.3 Intraclass Correlation Coefficient

Since the ICC analysis method is used to analyze differences in variance between various objects (62), in this case phantoms, consideration should be given to the effect the above mentioned possible outlier might have had on the ICC result for the VFA method. The possible outlier can be expected to have had an influence on the ICC result for the VFA method, as reliability tests like ICC are sensitive to outliers (68). As can be seen in table 5, the result of the ICC analysis of the VFA measurements would have been quite different, had the possible outlier been excluded from the analysis. An ICC value of 0.994, with a confidence interval of 0.968/0.999 is considered to have high (61) or almost perfect agreement (69). As it stands, an ICC value of 0,723 is still considered to represent a moderate correlation (61, 70), even though the term “moderate” can be hard to interpret. Depending on the source, an ICC of 0,723 can be considered moderate (61) or substantial (69, 70), which makes interpretation difficult. However, an ICC value of 0,723 could indicate the VFA method is a somewhat reliable method, although a repetition of the experiment could add further data to the analysis which might give a more conclusive result.

Apart from a repetition of the experiment to generate more data, the choice of ICC result type is also worthy of note. As can be seen in Table 3 and 4, the ICC values for Single Measures were chosen as the reported results. It is a more conservative option than the Average Measures results, and for the IR method, it makes no difference. But for the VFA method, there is a difference. The

Single Measures result compares the data points for each phantom with each other and bases its analysis on these values, whereas the Average Measures technique uses a mean of the values for each phantom and compares the measurements to that mean. The Average Measures will always give a higher ICC value than the Single Measures (71), which is why the Single Measures result can be seen as a conservative estimate. Since the ICC method has received criticism from several sources (61, 65), a conservative approach to the interpretation of the ICC results could be justified. There is also the possibility that the ICC value found in this report is overestimated, in a clinical context, as the T1 relaxation times for the phantoms do not all reflect relevant T1 relaxation times found in tissues. As the ICC method measures the probability of the data points as belonging to the same rank, a wide spread of the T1 relaxation times within the phantoms will increase the probability of getting an ICC value close to 1. Had the phantoms been created with T1 relaxation times closer to each other, a lower ICC value might have been the result.

There are other methods to examine correlation, which could be used. Within the ICC methodology there are several models with which an ICC value can be calculated. Although each ICC model gives a different ICC value, the most important thing when choosing a specific method is to describe it thoroughly, and regardless of the ICC model of choice, an ICC value close to 1 always indicates good reliability. (61) The Bland-Altman plot shows limits of agreement, marked on the plot as the mean \pm 2.46 X SD. As mentioned previously, the data might be interpreted as heteroscedastic, which could present a problem regarding the use of a residual regression method. An assumption associated with the regression method is that the residuals are homoscedastic and if they are not, it could have serious consequences (72), and the interpretation of the residual regression Bland-Altman plot should reflect this fact.

9.3 Results Comparison

Several scientific publications address the issue of comparing one or more flip angle methods with the golden standard IR method. In an experiment performed on a 3.0T scanner, the results indicated that the flip angle method had a good correlation with the IR golden standard, although the two methods did not exhibit good agreement (8). A review study in which data from several sources regarding the IR and VFA methods have been compiled, the results show that the VFA method overestimated the T1 relaxation time on a consistent basis (9). Those results correspond partially with the results found in this report. The T1 relaxation times examined in the review do not test several different T1 relaxation times, as only T1 times around 1000ms are reported. However, in

that T1 range, the results correspond with the results in this report. Around 500ms, the VFA and IR values found in this report are almost the same. At higher T1 times the VFA estimates are consistently overestimated, and at lower T1 times, the T1 times are consistently underestimated, as can be seen in appendix 8. This can also be observed graphically in graph 2, where the lower value T1 measurements lie beneath the identity line and the higher measurements lie above. Finding sources which investigate the very short relaxation times was not possible, which could indicate that these T1 relaxation times might not be clinically relevant.

9.4 Radio Frequency Field Inhomogeneity

The impact of RF field inhomogeneity when using the VFA method rises with increasing external magnetic field strengths, especially for scanners with a stronger field than 1.5T (8). This phenomenon constitutes a fundamental problem when quantifying MRI parameters, and could possibly have had an influence on the results in this report, as RF field inhomogeneity has a strong impact on image quality (8, 49). However, as explained in the method section, it was not possible to get information on the RF field inhomogeneities while conducting the experiments associated with this report, and, as such, remain an unknown variable associated with the evaluation of the results. Another problem associated with various RF field mapping techniques is the time required to do execute them (8), which might limit its feasibility in a clinical context. Flip angle scans executed without corrections for RF field inhomogeneities result in T1 relaxation times which are significantly underestimated in comparison to the IR golden standard (8).

9.5 Choice of Flip Angles

The flip angles used in this report were predetermined, and the reasoning and calculations behind them are unclear. However, since the T1 relaxation time of the phantom being scanned is an important factor in choosing optimal flip angles (8), it seems reasonable that a single set of flip angles does not match the IR curve across a variety of phantoms with different T1 relaxation times, ranging from a mean IR T1 time of 2788ms in phantom one to 83ms in phantom six, based on the data in appendix 8. The TR chosen for the flip angles is also an important parametric component when creating the optimal flip angle scan sequence (8), and the TR values used in this report were also predetermined. Since the optimal flip angles depend on the T1 relaxation time of the subject being scanned (8), it would be incorrect to assume that the differences between the IR and VFA measurements are solely due to possible programming errors found in Imalytics, possible scanner

inconsistencies or any systematic errors. The differences can be assumed to occur in any scanned subject with a T1 relaxation time unsuited for the predetermined protocol used in this report.

9.6 Alternative Scanning Methods

Although the spin echo inversion recovery technique is considered the golden standard when calculating T1 relaxation times (8, 12, 13), other techniques might have been considered for comparison with the 6 degree and 16 degree VFA method. Since the time scale required for using the gold standard IR method is unfeasible in a clinical context, faster ways to determine the T1 relaxation time have been explored, and can be divided into two categories: VFA technique and fast sampling of the IR curve (51). Look Locker (LL) (8, 51) and Modified Look Locker Inversion Recovery (MOLLI) can be used as well to determine T1 relaxation times (8, 12), and both involve fast sampling of the inversion recovery curve. The LL technique was created to address the issue of scan time when using IR, and its fundamental principle consists of sampling the IR curve multiple times during a single inversion, compared to only one sampling with the traditional IR technique. However, the LL technique suffers from inaccuracies, which can result in an underestimation of the T1 relaxation time. (8, 51) The MOLLI method is a more complex version of the LL technique. It has shown a high grade of accuracy and reproducibility (8, 73) , and produce T1 relaxation times which are in better agreement with the IR T1 relaxation times compared to the LL method when the measurements are conducted on phantoms (8). However, the interest of the MOLLI sequence might not be relevant in relation to cancer, as a search in PubMed and Web of Science using the search words “MOLLI AND MRI AND cancer” yielded no results in both search engines. The scientific publications about MOLLI found during the making of this report are all exclusively about T1 mapping of the heart. However, using either the LL or MOLLI method as a basis for comparison with the VFA method is questionable, as neither technique offers T1 relaxation times in consistent agreement with the golden standard IR technique over a range of T1 values ranging from around 100ms to 3500ms (8).

Even though T1 relaxation times for different tissue types, as well as water phantoms with different concentrations of gadolinium CAs can be found in the literature, it is still a necessity to determine accurately the T1 relaxation times on each individual scanner. Even though scanners might have the same external magnetic field strength, are the same subtype of scanner and is made by the same manufacturer, the T1 relaxation times are not necessarily the same. (12) This fact highlights the need for a determination of the T1 relaxation times associated with the specific scanner used for

generating the data used this report, as it will also be used for future projects involving DCE-MRI image quantification.

9.7 Imalytics

The use of the Imalytics software was an iterative process, conducted in collaboration between Philips and the Department of Medical Physics. The software is not a finished product, and several changes were made to the software, based on the data and images used in this report. The version of the software, which was in effect when the T1 relaxation times for this report were generated was based on corrections made by Philips as a result of an earlier analysis of the MRI images used in this report. As the final data was generated, the software seemed to operate as intended, creating relaxation maps with relevant T1 relaxation times. However, DCE-MRI images of pig brains were later processed with the software by the department MRI physicist, and the software did not produce T1 relaxation maps which were in accordance with known reference T1 values for brain tissue. The results presented in this report should therefore be evaluated with consideration to the incomplete state of the Imalytics software and its unknown reliability regarding the creation of T1 relaxation maps.

10.0 Conclusion

The results from this study show that the VFA generated T1 relaxation maps created with Imalytics exhibited moderate reliability (ICC = 0,723), although still less reliable than the IR method (ICC = 1). The mean precision of the VFA method was less than it was for the IR method, with a CV of the former being 12.15% and the CV of the latter being 0.82%. However, both the ICC value and the mean CV value for the VFA method might be underestimated due to sample contamination, as a possible outlier is included in the analysis.

11.0 Future Prospects

A number of projects could be conducted to further investigate the use of the VFA technique for T1 mapping. Finding the optimal clinical flip angles, based on the estimated T1 value of the tissue of interest would be of clinical value, as this could provide an anatomically specific map for different parts of the human body, for example the brain. Creating water/gadolinium phantoms with T1 relaxation times in the same range as a desired type of brain tissue could be used to identify the optimal VFAs. The method could further be tested by performing VFA scans on pig brains or voluntary human subjects. Further studies into the importance of different TR and TE values and their effects on the VFA generated T1 relaxation maps would also be an area of research which could improve the method.

Earlier in the report, some concerns were expressed regarding a possible outlier and its effect on the final results. As there were no clear evidence that the data point was undoubtedly an outlier, a repetition of the VFA part of the experiment might shed further light on the matter. If this second experiment generated data which were in agreement with the data set used in this report, disregarding the possible outlier, it would create further evidence that the possible outlier was indeed a true outlier. Such an experiment could increase the validity of the estimated precision of the VFA method.

As mentioned in the discussion, there is a probability that the ICC values found in this report are overestimated, due to the fact that the T1 relaxation times of the phantoms were very far apart and not all of them were clinically relevant. To gain further insight into the reliability of both the VFA and IR methods, new phantoms could be created with T1 relaxation times closer to each other, and in a range that would be more relevant in a clinical context.

As mentioned in the discussion, the MOLLI T1 mapping technique was only found to be used in the context of T1 relaxation maps of the heart. Since the technique shows promise with its high accuracy and reproducibility (8, 73), it might be of interest to test the technique in relation to cancer patients. The MOLLI technique might show further promise in relation to cerebral cancers, as the technique exhibits excellent agreement with the gold standard IR method around 1200ms (8), which is reasonably close to the T1 relaxation times for both white brain matter (1010ms) and grey brain matter (1200ms), according to table 2. An initial validation of these relaxation times might be needed, as the T1 value for white brain matter can differ substantially across scanners, even though they possess the same external magnetic field strength (9). Although the specific scanner used in

this report have listed T1 relaxation times for different tissue types, a validation might still be necessary, as the scanner also lists T1 relaxation times for other field strengths, which indicates that the listed values are not based on measurements performed on the specific scanner. Since the listed values regarding 3.0T are for “3.0T systems” (table 2), one could speculate that the individual values might be based on a mean, perhaps calculated from data gathered from a number of scanners.

The Department of Medical Physics have recently acquired a license for another quantitative image handling program, called nordicICE. A study regarding the reliability and precision of this program in creating T1 relaxation maps could prove valuable, and could provide an alternative to Imalytics.

12.0 References

1. de Groot JF, Mandel JJ. Update on anti-angiogenic treatment for malignant gliomas. *Current oncology reports*. 2014;16(4):380.
2. Larsen VA, Simonsen HJ, Law I, Larsson HB, Hansen AE. Evaluation of dynamic contrast-enhanced T1-weighted perfusion MRI in the differentiation of tumor recurrence from radiation necrosis. *Neuroradiology*. 2013;55(3):361-9.
3. Larsson HB, Courivaud F, Rostrup E, Hansen AE. Measurement of brain perfusion, blood volume, and blood-brain barrier permeability, using dynamic contrast-enhanced T(1)-weighted MRI at 3 tesla. *Magnetic resonance in medicine : official journal of the Society of Magnetic Resonance in Medicine / Society of Magnetic Resonance in Medicine*. 2009;62(5):1270-81.
4. Collins DJ, Padhani AR. Dynamic magnetic resonance imaging of tumor perfusion. 2004.
5. Zahra MA, Hollingsworth KG, Sala E, Lomas DJ, Tan LT. Dynamic contrast-enhanced MRI as a predictor of tumour response to radiotherapy. *The Lancet Oncology*. 2007;8(1):63-74.
6. Liu G, Rugo HS, Wilding G, McShane TM, Evelhoch JL, Ng C, et al. Dynamic contrast-enhanced magnetic resonance imaging as a pharmacodynamic measure of response after acute dosing of AG-013736, an oral angiogenesis inhibitor, in patients with advanced solid tumors: results from a phase I study. *Journal of clinical oncology : official journal of the American Society of Clinical Oncology*. 2005;23(24):5464-73.
7. Treier R, Steingoetter A, Fried M, Schwizer W, Boesiger P. Optimized and combined T1 and B1 mapping technique for fast and accurate T1 quantification in contrast-enhanced abdominal MRI. *Magnetic resonance in medicine : official journal of the Society of Magnetic Resonance in Medicine / Society of Magnetic Resonance in Medicine*. 2007;57(3):568-76.
8. Zhou X. Myocardial T1 mapping techniques for quantification of myocardial fibrosis. 2012.
9. Stikov N, Boudreau M, Levesque IR, Tardif CL, Barral JK, Pike GB. On the accuracy of T mapping: Searching for common ground. *Magnetic resonance in medicine : official journal of the Society of Magnetic Resonance in Medicine / Society of Magnetic Resonance in Medicine*. 2014.
10. Laustsen SR. Godkendelse af videregivelse af oplysninger fra patientjournaler til brug for forskningsprojektet: Funktionel magnetisk resonans-billeddannelse hos patienter med hjernetumorer (Project number: N-20130062). 2011.
11. Funktionel Magnetisk Resonans til Vurdering af 2. Linje Kemoterapi Effekt på Glioblasoma Multiforme (Project number: N-20140021; Den Nationale Videnskabetiske Komité). 2014.
12. Raman FS, Kawel-Boehm N, Gai N, Freed M, Han J, Liu CY, et al. Modified look-locker inversion recovery T1 mapping indices: assessment of accuracy and reproducibility between magnetic resonance scanners. *Journal of cardiovascular magnetic resonance : official journal of the Society for Cardiovascular Magnetic Resonance*. 2013;15:64.
13. Trzasko JD, Mostardi PM, Riederer SJ, Manduca A. Estimating T1 from multichannel variable flip angle SPGR sequences. *Magnetic resonance in medicine : official journal of the Society of Magnetic Resonance in Medicine / Society of Magnetic Resonance in Medicine*. 2013;69(6):1787-94.

14. Voglein J, Tuttonberg J, Weimer M, Gerigk L, Kauczor HU, Essig M, et al. Treatment monitoring in gliomas: comparison of dynamic susceptibility-weighted contrast-enhanced and spectroscopic MRI techniques for identifying treatment failure. *Investigative radiology*. 2011;46(6):390-400.
15. Wolbers JG. Novel strategies in glioblastoma surgery aim at safe, supra-maximum resection in conjunction with local therapies. *Chinese journal of cancer*. 2014;33(1):8-15.
16. Chen C, Huang R, MacLean A, Muzikansky A, Mukundan S, Wen PY, et al. Recurrent high-grade glioma treated with bevacizumab: prognostic value of MGMT methylation, EGFR status and pretreatment MRI in determining response and survival. *Journal of neuro-oncology*. 2013;115(2):267-76.
17. Dhermain F. Radiotherapy of high-grade gliomas: current standards and new concepts, innovations in imaging and radiotherapy, and new therapeutic approaches. *Chinese journal of cancer*. 2014;33(1):16-24.
18. White E, Bienemann A, Pugh J, Castrique E, Wyatt M, Taylor H, et al. An evaluation of the safety and feasibility of convection-enhanced delivery of carboplatin into the white matter as a potential treatment for high-grade glioma. *Journal of neuro-oncology*. 2012;108(1):77-88.
19. Quick J, Gessler F, Dutzmann S, Hattingen E, Harter PN, Weise LM, et al. Benefit of tumor resection for recurrent glioblastoma. *Journal of neuro-oncology*. 2014;117(2):365-72.
20. Kosztyla R, Chan EK, Hsu F, Wilson D, Ma R, Cheung A, et al. High-grade glioma radiation therapy target volumes and patterns of failure obtained from magnetic resonance imaging and 18F-FDOPA positron emission tomography delineations from multiple observers. *International journal of radiation oncology, biology, physics*. 2013;87(5):1100-6.
21. Hu LS, Eschbacher JM, Heiserman JE, Dueck AC, Shapiro WR, Liu S, et al. Reevaluating the imaging definition of tumor progression: perfusion MRI quantifies recurrent glioblastoma tumor fraction, pseudoprogression, and radiation necrosis to predict survival. *Neuro-oncology*. 2012;14(7):919-30.
22. Cabrera AR, Cuneo KC, Desjardins A, Sampson JH, McSherry F, Herndon JE, 2nd, et al. Concurrent stereotactic radiosurgery and bevacizumab in recurrent malignant gliomas: a prospective trial. *International journal of radiation oncology, biology, physics*. 2013;86(5):873-9.
23. Shah AH, Snelling B, Bregy A, Patel PR, Tememe D, Bhatia R, et al. Discriminating radiation necrosis from tumor progression in gliomas: a systematic review what is the best imaging modality? *Journal of neuro-oncology*. 2013;112(2):141-52.
24. Lemasson B, Chenevert TL, Lawrence TS, Tsien C, Sundgren PC, Meyer CR, et al. Impact of Perfusion Map Analysis on Early Survival Prediction Accuracy in Glioma Patients. *Translational oncology*. 2013;6(6):766-74.
25. Chinot OL, Macdonald DR, Abrey LE, Zahlmann G, Kerloeguen Y, Cloughesy TF. Response assessment criteria for glioblastoma: practical adaptation and implementation in clinical trials of antiangiogenic therapy. *Current neurology and neuroscience reports*. 2013;13(5):347.
26. Trevisan E, Bertero L, Bosa C, Magistrello M, Pellerino A, Ruda R, et al. Antiangiogenic therapy of brain tumors: the role of bevacizumab. *Neurological sciences : official journal of the Italian Neurological Society and of the Italian Society of Clinical Neurophysiology*. 2014;35(4):507-14.

27. Zhou R, Pickup S, Yankeelov TE, Springer CS, Jr., Glickson JD. Simultaneous measurement of arterial input function and tumor pharmacokinetics in mice by dynamic contrast enhanced imaging: effects of transcytolemmal water exchange. *Magnetic resonance in medicine : official journal of the Society of Magnetic Resonance in Medicine / Society of Magnetic Resonance in Medicine*. 2004;52(2):248-57.
28. Zhang X, Pagel MD, Baker AF, Gillies RJ. Reproducibility of Magnetic Resonance Perfusion Imaging. 2014.
29. Moeller BJ, Dreher MR, Rabbani ZN, Schroeder T, Cao Y, Li CY, et al. Pleiotropic effects of HIF-1 blockade on tumor radiosensitivity. *Cancer cell*. 2005;8(2):99-110.
30. Price SJ. The role of advanced MR imaging in understanding brain tumour pathology. *British journal of neurosurgery*. 2007;21(6):562-75.
31. Fatterpekar GM, Galheigo D, Narayana A, Johnson G, Knopp E. Treatment-related change versus tumor recurrence in high-grade gliomas: a diagnostic conundrum--use of dynamic susceptibility contrast-enhanced (DSC) perfusion MRI. *AJR American journal of roentgenology*. 2012;198(1):19-26.
32. Messroghli DR, Niendorf T, Schulz-Menger J, Dietz R, Friedrich MG. T1 Mapping in Patients with Acute Myocardial Infarction. *Journal of Cardiovascular Magnetic Resonance*. 2003;5(2):353-9.
33. Dietrich O, Freiermuth M, Willerding L, Reiser MF, Peller M. Flip angle-optimized fast dynamic T mapping with a 3D gradient echo sequence. *Magnetic resonance in medicine : official journal of the Society of Magnetic Resonance in Medicine / Society of Magnetic Resonance in Medicine*. 2014.
34. Manuel A, Li W, Jellus V, Hughes T, Prasad PV. Variable flip angle-based fast three-dimensional T1 mapping for delayed gadolinium-enhanced MRI of cartilage of the knee: need for B1 correction. *Magnetic resonance in medicine : official journal of the Society of Magnetic Resonance in Medicine / Society of Magnetic Resonance in Medicine*. 2011;65(5):1377-83.
35. Bushberg JT, Seibert JA, Jr. EML, Boone JM. *The Essential Physics of Medical Imaging*, chap. 14. 2nd Edition. 2002.
36. <http://electron6.phys.utk.edu/phys250/modules/module%203/nmr.htm> (Visited 24/4 - 2014).
37. Hashemi RH, Jr. WGB, Lisanti CJ. *MRI, The Basics*, chap. 4. 2010.
38. Hashemi RH, Jr. WGB, Lisanti CJ. *MRI, The Basics*, chap. 2. 2010.
39. Westbrook C, Roth CK, Talbot J. *MRI in Practice*, chap. 9, 4th Edition. 2011.
40. Geraldes CF, Laurent S. Classification and basic properties of contrast agents for magnetic resonance imaging. *Contrast media & molecular imaging*. 2009;4(1):1-23.
41. <http://www.drugs.com/pro/dotarem.html> (Visited 28/4 - 14. Last revised: June 2013).
42. <http://www.mr-tip.com/serv1.php?type=db1&db=Extracellular+Fluid+Agents> (Visited 28/4 - 14).
43. Chen BB, Shih TT. DCE-MRI in hepatocellular carcinoma-clinical and therapeutic image biomarker. *World journal of gastroenterology : WJG*. 2014;20(12):3125-34.
44. Aksoy D, Bammer R, Mlynash M, Venkatasubramanian C, Eyngorn I, Snider RW, et al. Magnetic resonance imaging profile of blood-brain barrier injury in patients with acute intracerebral hemorrhage. *Journal of the American Heart Association*. 2013;2(3):e000161.

45. Shin KE, Ahn KJ, Choi HS, Jung SL, Kim BS, Jeon SS, et al. DCE and DSC MR perfusion imaging in the differentiation of recurrent tumour from treatment-related changes in patients with glioma. *Clinical radiology*. 2014;69(6):e264-72.
46. Tofts PS, Brix G, Buckley DL, Evelhoch JL, Henderson E, Knopp MV, et al. Estimating kinetic parameters from dynamic contrast-enhanced T(1)-weighted MRI of a diffusable tracer: standardized quantities and symbols. *Journal of magnetic resonance imaging : JMRI*. 1999;10(3):223-32.
47. Bernstein MA, King KF, Zhou XJ. *Handbook of MRI Pulse Sequences*, section 14.2.1. 2004.
48. Westbrook C, Roth CK, Talbot J. *MRI in Practice*, chap. 5, 4th Edition. 2011.
49. Sung K, Saranathan M, Daniel BL, Hargreaves BA. Simultaneous T(1) and B(1) (+) mapping using reference region variable flip angle imaging. *Magnetic resonance in medicine : official journal of the Society of Magnetic Resonance in Medicine / Society of Magnetic Resonance in Medicine*. 2013;70(4):954-61.
50. Hashemi RH, Jr. WGB, Lisanti CJ. *MRI, the Basics*, chap. 20. 2010.
51. Hui C, Esparza-Coss E, Narayana PA. Improved three-dimensional Look-Locker acquisition scheme and angle map filtering procedure for T1 estimation. *NMR in biomedicine*. 2013;26(11):1420-30.
52. Balezeau F, Eliat PA, Cayamo AB, Saint-Jalmes H. Mapping of low flip angles in magnetic resonance. *Physics in medicine and biology*. 2011;56(20):6635-47.
53. Preim B, Bartz D. *Visualization in Medicine: Theory, Algorithms, and Applications*, chap 1 part II. 2007.
54. Rane SD, Gore JC. Measurement of T1 of human arterial and venous blood at 7T. *Magnetic resonance imaging*. 2013;31(3):477-9.
55. <http://www.drugs.com/newdrugs/fda-approves-dotarem-new-magnetic-resonance-imaging-agent-3728.html> (Visited 19/3 - 2014. Last revised: March 2013).
56. http://web.eecs.umich.edu/~dnoll/BME516/phys_movies_516.pdf (Visited 2/5 - 2014).
57. Bernstein MA, King KF, Zhou XJ. *Handbook of MRI Pulse Sequences*, section 14.1.1. 2004.
58. Bernstein MA, King KF, Zhou XJ. *Handbook of MRI Pulse Sequences*, page 609, equation 14.31. 2004.
59. <http://www.philips.com/e/imalytics/productsnew/imalytics.html> (Visited 2/5 - 2014).
60. <http://www.adasis-oz.com/tips/2013/8/28/what-is-the-intra-class-correlation-coefficient> (Visited 20/5 - 2014).
61. Atkinson G, Nevill AM. Statistical methods for assessing measurement error (reliability) in variables relevant to sports medicine. *Sports medicine (Auckland, NZ)*. 1998;26(4):217-38.
62. McGraw KO, Wong SP. *Forming Inferences About Some Intraclass Correlation Coefficients*. 1996.
63. Giraudeau B. Negative Values of the Intraclass Correlation Coefficient Are Not Theoretically Possible 1996.
64. Zar JH. *Biostatistical Analysis*. Zar JH, editor: Indianapolis, Ind. : Prentice Hall; Pages 41-42. . 2008.
65. Bland JM, Altman DG. *Measuring Agreement in Method Comparison Studies*. 1999.
66. Zar JH. *Biostatistical Analysis*. Zar JH, editor: Indianapolis, Ind. : Prentice Hall; Pages 19-20. 2008.

67. Zar JH. Biostatistical Analysis. Zar JH, editor: Indianapolis, Ind. : Prentice Hall; Page 360. 2008.
68. http://www.gmat.unsw.edu.au/snap/gps/gps_survey/chap2/241relb.htm (Visited 25/5 - 2014. Last updated: 1999).
69. http://www.kcl.ac.uk/iop/depts/biostatistics/SAS/faqs9.aspx#a9_10 (Visited 26/5 - 2014).
70. Zou GY. Sample size formulas for estimating intraclass correlation coefficients with precision and assurance. *Statistics in medicine*. 2012;31(29):3972-81.
71. <http://www.medcalc.org/manual/intraclasscorrelation.php> (Visited 26/5 - 2014).
72. Bowers D. *Medical Statistics From Scratch*, 2. edition, Pages 195-196. 2008.
73. Shao J, Nguyen KL, Natsuaki Y, Spottiswoode B, Hu P. Instantaneous signal loss simulation (InSiL): An improved algorithm for myocardial T mapping using the MOLLI sequence. *Journal of magnetic resonance imaging : JMRI*. 2014.